


# Advanced analysis of fan noise measurements supported by theoretical source models

International Journal of Aeroacoustics  
2022, Vol. 0(0) 1–21  
© The Author(s) 2022



Article reuse guidelines:  
[sagepub.com/journals-permissions](https://sagepub.com/journals-permissions)  
DOI: 10.1177/1475472X221093703  
[journals.sagepub.com/home/jae](https://journals.sagepub.com/home/jae)



Lukas Klähn\* , Antoine Moreau, Luciano Caldas, Robert Jaron and Ulf Tapken

## Abstract

With the objective to improve the understanding of the dominant fan noise source mechanisms, a comprehensive experimental study was conducted at a low speed fan test rig. The aerodynamic fan map as well as the acoustic characteristics of the fan was measured for a new blade integrated disk (Blisk) rotor with systematic variation of the shaft speed and throttling. The interpretation of the results is supported by simulations of the experiment with a physics-based analytical in-house tool for fan noise prediction. For the acoustic measurements, an array of wall-flushed microphones was used in the inlet section. By means of radial mode analysis techniques, the broadband and tonal sound powers are calculated for each operating point. In the obtained comprehensive database, systematic variations of the tonal and broadband sound power with the flow rate are found. These patterns can only partly be correlated to the varying incidence angle of the rotor blades. Comparing the mode distributions of the measured noise and the analytical models then allows conclusions on the predominant noise sources of rotor–stator interaction and inflow–rotor interaction.

## Keywords

Fan noise, analytical prediction, radial mode analysis, microphone array measurements, inflow–rotor interaction, rotor–stator interaction

Date received: 2 December 2021; revised: 19 October 2021; accepted: 6 March 2022

## Introduction

The goal of the present work is to assess the impact of different fan operating points on fan noise generation. For that purpose, a comprehensive experimental study was performed in a small-scale

---

Engine Acoustics Department, German Aerospace Center (DLR), Berlin, Germany

### Corresponding author:

\*Lukas Klähn, German Aerospace Center (DLR), Institute of Propulsion Technology, Engine Acoustics Department, Müller-Breslau-Str. 8, Berlin 10623, Germany.

Email: [Lukas.Klaehn@dlr.de](mailto:Lukas.Klaehn@dlr.de)

low-speed aeroacoustic fan test rig.<sup>1</sup> The fan aerodynamic performance map and its acoustic characteristics were assessed by measuring the fan at several operating points. The test rig is equipped with a new blade integrated disk rotor (Blisk). This type of rotor is milled from one piece, enabling virtually unlimited variations in the blade number and reducing the number of assembly parts. Thus, also the weight can be significantly reduced.<sup>2</sup> From an aerodynamic and aeroacoustic point of view, the arbitrary shape opens new optimization spaces, but most evident is the improvement of the flow properties at the hub, where there are no gaps that can affect the flow.

The experimental study is accompanied by calculations with an analytical fan noise prediction method.<sup>3</sup> In previous studies, this method has been used for acoustic optimization in the design process of turbofans<sup>4–6</sup> and helped to derive noise reduction measures.<sup>7</sup>

In the present paper, the analytical method is used to help analyze the measured sound radiation upstream of an existing model fan. The measurements were simulated on the basis of the measured flow parameters and different noise sources were calculated. First results showed that the dominant sources that radiate in upstream direction are the inflow-rotor interaction and the tonal and broadband rotor–stator interaction (RSI); hence, we focus on these sources.

The interdependency of fan design, loading condition, and fan noise has been the topic of manifold experimental, analytical, and numerical studies, some are found in Refs. 3, 4, and 8–11. While the source of tonal RSI noise is well known since the study of Tyler and Sofrin,<sup>12</sup> it is still the subject in recent studies. The propagation and radiation properties of the fully correlated tonal RSI noise behave very sensitively to changes in the operating conditions or geometry.<sup>6,10</sup>

While it is known that the broadband noise increases with the fifth power of the rotor speed,<sup>3,9,11</sup> the correlation between fan loading and broadband noise is more complex.<sup>8,9,13</sup> Decomposition into radial modes of measured broadband noise showed that the sound power can in fact not be assumed to be a uniform distribution over the duct modes and frequencies. On the contrary, an asymmetry of the mode spectrum was found as well as frequency bands with elevated sound power, that were not always related to cut-on frequencies of duct modes.<sup>1</sup>

The authors see the need for further research and advanced analysis techniques, to interpret the results of in duct measurements and to trace the findings back to specific noise source mechanisms as this is a prerequisite to develop noise reduction measures.<sup>7</sup> This paper provides a systematic parameter study with the objective to identify specific sources on the basis of their respective radiated mode pattern. For that purpose, established mode analysis techniques are applied on a comprehensive set of measurement data, enabling accurate computations of the modal sound power for a variation of loading conditions. By combining the experimental results with the modeled noise sources, the contribution of these sources is evaluated.

In the scope of this paper, the test rig and model fan are briefly described and an outline of the signal processing chain is given. The experimentally determined tonal and broadband sound powers at varying loading conditions are then presented. Finally, the behavior of different noise sources at varying loading conditions is physically interpreted with the help of physics-based source models. Thus, the complex behavior of the measured broadband sound power at varying loading conditions is traced back to the superposition of the inflow-rotor interaction and the broadband RSI noise sources.

## Experimental Setup

The test rig is described in the next subsection, followed by a brief description of the Blisk rotor.

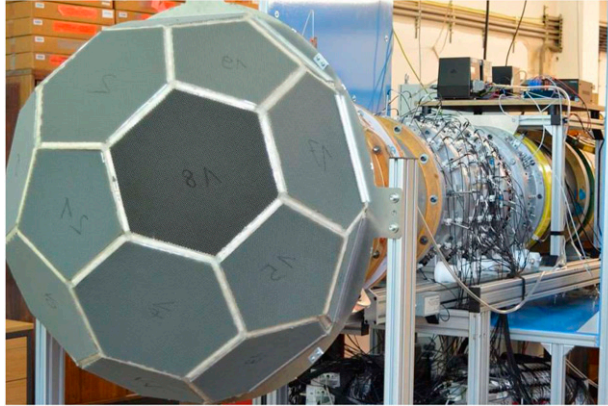


**Figure 1.** Overview of the test rig and the used ICD.

*Fan Test Rig.* Experiments were performed in a small-scale low-speed fan stage test rig with a conventional rotor–stator arrangement without core stream. A Blisk rotor was designed to provide an optimized performance in combination with an already existing stator. All measurements were performed in the duct with a diameter of 453.6 mm. In order to reduce inflow distortions, a simplified inflow control device (ICD) was attached to the bell mouth (see Figure 1). The test rig is located in a laboratory environment with no special acoustic or aerodynamic treatment, except for the abovementioned ICD.

The turbulence intensity and the non-stationary and non-homogeneous inflow distortions are reduced significantly compared to the measurement without ICD as was shown by Oertwig.<sup>14</sup> Downstream of the bell mouth, in a nozzle the diameter is reduced to match the rotor diameter. The acoustic measurement section is located between the rotor casing and the inlet nozzle (see Figure 2).

The microphones are mounted wall flushed in six ring arrays and one line array. The first three rings (from left to right) are equipped with 18, the fourth and fifth rings with 24, and the sixth ring with 36 microphones, that are uniformly distributed in azimuthal direction, respectively. Additionally, a line array is used with 23 equally spaced microphones, except for two gaps caused by the duct flanges. Downstream of the stator follow a diffuser, the outlet measurement section, an anechoic outlet, and the throttle, that is used to adjust the operating point; this allows a systematic parameter variation. Further information on the test rig can be found in reference.<sup>1</sup>

*Blade-Integrated Disk Rotor.* The integrated disk rotor was designed with the goal of achieving a representative configuration in terms of relative Mach numbers and without flow detachments. The design boundary conditions are given by the rig maximum rotational speed of 3200 r/min, the flow channel outer and inner diameter, and the already existing stator consisting of  $V = 32$  curved plates with an inflow angle of  $34^\circ$ . The blade count was chosen as  $B = 18$ . Following the findings of Tyler and Sofrin,<sup>12</sup> the rotor–stator interaction mode of the first BPF is cut off at the design operating point. This means that the mode that is excited due to the phase relations between the rotor wakes and stator leading edges with azimuthal mode order  $m = V - B = 14$  does not propagate in upstream direction but decays exponentially. For the design of the blade shape, a semi-analytical approach for the design of low-Mach number fans developed by Jaron<sup>15</sup> was used.

In this approach, NACA65 profiles are generated discretely distributed along the span (see Figure 3(a)) by using the correlations empirically found by Lieblein<sup>16</sup> regarding the design

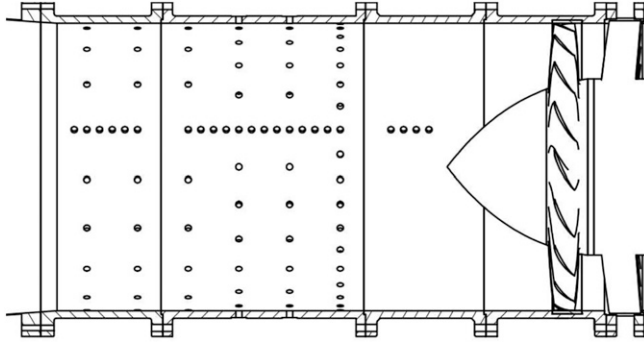


**Figure 2.** Acoustic measurement section and Blisk rotor.

incidence, deviation, and lift coefficient. By stacking the profiles along their center of gravity, a 3D blade shape is generated (see Figure 3(b)). The vortex design was manually adapted to fit the constant inflow angle of the stator. The aerodynamic stability is ensured by using the empirical blade loading criteria of de Haller<sup>17</sup> and Lieblein.<sup>18</sup>

The aerodynamic efficiency and the mechanical stability of the final design (see Figure 3(c)) were validated by means of CFD and FEM simulations, respectively. The flow simulation showed no rotor flow detachment and a stator inflow angle without significant incidence. The mechanical simulation confirmed that the occurring highest static stress has a sufficient safety factor.

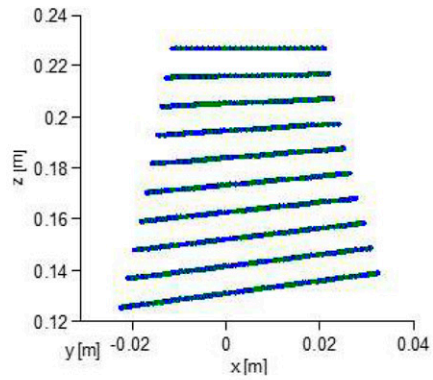
**Aerodynamic fan map.** The aerodynamic operating conditions were measured by means of a Pitot tube in the inlet, and four circumferentially distributed static pressure holes in the inlet and the outlet section of the test rig. The total pressure upstream and downstream of the fan is calculated considering the ambient pressure and air density  $\rho$  in the laboratory. The performance map in terms of the ISA sea-level corrected value for the mass flow  $Q_{\text{corr}}$  and total pressure ratio  $PR$  is shown in Figure 4.

The small grey dots indicate aerodynamic measurements, while the larger blue dots indicate operating points where acoustic measurements were also performed. For each of these points, 60 s of data sampled at 50 kHz was simultaneously acquired using the inlet microphone array. Each fan operation point was set with the help of a throttle device. By setting its axial position at the rig's exhaust, the mass-flow can be adjusted. By doing that, different flow coefficients can be established. In order to address the impact of fan loading on fan acoustics, in this work six flow coefficients were measured and analyzed. The flow coefficient is a non-dimensional ratio of the axial flow speed and the rotor tip speed defined by

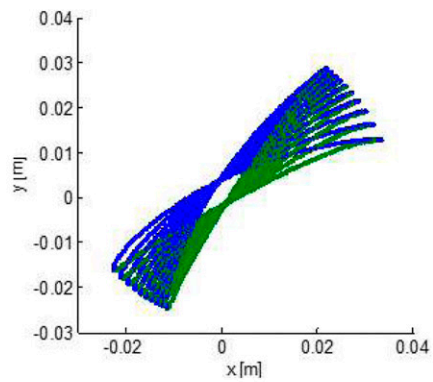
$$\phi = \frac{M_{\text{in}}}{M_{\text{tip}}} \quad (1)$$

where  $M_{\text{in}}$  is the axial Mach number in the inlet section and  $M_{\text{tip}}$  is the blade tip Mach number.

In Table 1, the fan-operating points are numerated with respect to the rotor speed and the flow coefficient. For example, the fan design point (marked in Figure 4 by a red diamond symbol), found at rotor speed of 3200 r/min and the flow coefficient  $\phi = 0.24$ , is abbreviated as operating point 3200E.



(a) Spanwise distribution of the profiles.



(b) Profiles stacked along their center of gravity.



(c) Blade integrated disk rotor mounted on the Flocon test rig.

**Figure 3.** Design of the blade integrated disk rotor.

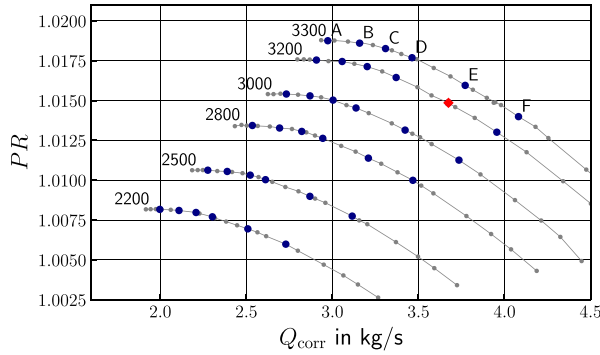


**Figure 4.** Performance map of the operating points.

**Table I.** Abbreviation letters for the operating points.

	A	B	C	D	E	F
$\phi$	0.19	0.20	0.21	0.22	0.24	0.26

### Signal Processing

The signals are firstly resampled using the rotor trigger signal as reference. This approach compensates fluctuations of the rotor speed and suppresses incoherent pressure fluctuations.<sup>19</sup> Signals are subsequently split with the help of a cyclostationary analysis into: one part with a locked phase relative to the rotor, and a second with the fluctuating component.<sup>20,21</sup> Through this averaging procedure in the time domain, only pure tones remain in the rotor-locked spectrum. It is therefore also referred to as tonal spectrum. The fluctuating spectrum contains rotor-incoherent fluctuations with random phase and is also referred to as broadband spectrum. The cross-power spectra  $S_{pq}$  for each combination of microphone positions are calculated for the fluctuating components.

As described comprehensively in Ref. 12, the sound field in a hard-wall annular duct with uniform axial mean flow can be represented as a superposition of acoustic modes. Each mode is characterized by its azimuthal and radial mode orders  $m$  and  $n$ , direction of propagation, wave number, and shape function. With these parameters, the modal amplitudes  $\mathbf{a}$  are linked with the sound pressure amplitudes at the microphone positions  $\mathbf{p}$ . This relation is represented by the mode transfer matrix  $\mathbf{W}$ .<sup>22</sup> The radial mode amplitudes  $A_{mn}^{\pm}$  for a fully correlated sound field, as is the case for the rotor-locked component, can be determined by solving the following equation

$$\mathbf{p} = \mathbf{W} \cdot \mathbf{a} \quad (2)$$

The noise sources and therefore also the propagating modes of the fluctuating components cannot be assumed to be fully correlated. The cross-modal matrix  $\mathbf{S}_{aa}$  can be calculated from the cross-spectral matrix of the microphone signals<sup>23</sup>

$$\mathbf{S}_{pp} = \mathbf{W} \cdot \mathbf{S}_{aa} \cdot \mathbf{W}^H \quad (3)$$

The least squares fit solution of equations (2) and (3) is calculated with the pseudo-inverse of the transfer matrix. The expected values of the squared-mode amplitudes are found on the diagonal of the cross-modal matrix. With the array used, a full radial mode decomposition up to 2000 Hz is

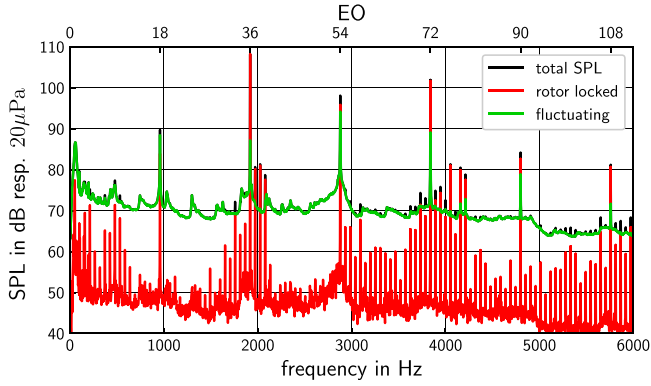


**Figure 5.** Averaged sound pressure level of all microphones separated into tonal (rotor-locked) and broadband (fluctuating) components at operating point 3200E.

accurate and robust for both the correlated and uncorrelated methods, as was shown by means of the condition number of the array.<sup>1</sup>

For the radiated noise, the acoustic energy that is transported by all propagating modes is crucial. The sound power of each mode  $P_{mn}^{\pm}$  is calculated individually at each frequency

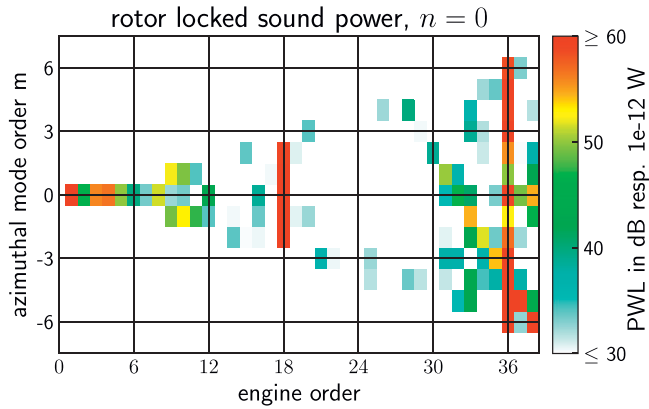
$$\langle P_{mn}^{\pm} \rangle = \frac{\pi R^2}{\rho c} \frac{\alpha_{mn} (1 - M_{in}^2)^2}{(1 \mp \alpha_{mn} M_{in})^2} \langle |A_{mn}^{\pm}|^2 \rangle \quad (4)$$

with  $\alpha_{mn}$  the mode cut-on factor,<sup>22</sup>  $R$  the duct radius, and  $c$  the speed of sound. The modal sound powers are summed to calculate the overall sound power.<sup>1,24</sup> An approach using only one azimuthal ring and one line of microphones has shown to increase the frequency range while the number of microphones is reduced.<sup>25</sup> This method can be of interest for further studies.

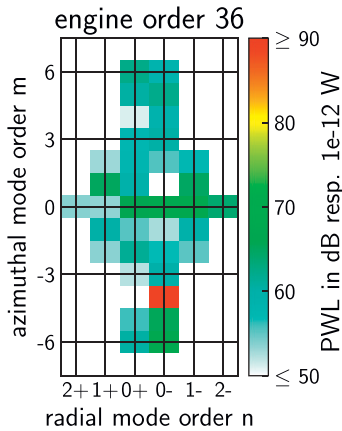
## Measurement Results

In this section, experimental results are exemplarily presented for the design operating point. As the rotor–stator interaction (RSI) mode of the BPF tone is cut off, the results of the parameter variation are presented for the sound power level at two BPF, the tone with highest amplitude, and the integrated broadband sound power level.

In Figure 5, the mean over the auto power spectra of all microphones is shown for the total signal, the tonal rotor-locked component, and the broadband-fluctuating component. The dominant tone is the second blade passing frequency. The rotor-locked component is about 20 dB above the fluctuating component. The RSI mode is excited by collisions of the rotor wakes with the stator leading edge. This source mechanism is rotor-coherent and is the reason for the high amplitude of the rotor-coherent two BPF tone. Thus, the rotor–stator interaction is identified as the source of this tone, which will also be confirmed in terms of a radial mode analysis further below. The first BPF is also excited, but for a large part with random phase relation to the rotor. This may be an indicator for remaining inflow distortions in the flow profile near the outer duct boundary which were not sufficiently equalized by the ICD.<sup>26</sup> Also visible are multiple pure tones above the second and fourth BPF. The third BPF is excited rather weakly. This can be linked to the propagation angle of the RSI mode at three BPF. Here the excited mode is of the azimuthal order  $m = 10$  and has a propagation



(a) Modal sound power of upstream propagating modes with radial order  $n = 0$ .



(b) Modal sound power at 2 BPF.

**Figure 6.** Modal decomposition of the sound field at test point 3200E.

angle of  $35.8^\circ$ , using Rices formula<sup>27</sup> and therefore is nearly parallel to the stator vane leading edge with an angle of  $34^\circ$ . This effect is explained with dipole-shaped sources on the stator leading edge: the dipole distribution cannot excite modes with a propagation angle perpendicular to the dipole axis.<sup>10,28</sup>

In the fluctuating component, a high SPL is visible around the first engine order. The authors suppose that this is related to the turbulent inflow rather than to the rotor. In the rotor-locked spectrum however also a tone at engine order one is visible, that is about 30 dB below the level of two BPF. This tone propagates in the form of a plane wave and is suspected to be radiated directly from the motor that is located inside the hub.

**Tonal Mode Analysis Results.** As the tonal spectrum only contains the rotor phase-locked components, solving equation (2) is applicable. In Figure 6(a), the result of a tonal RMA is visualized for the aerodynamic design point.



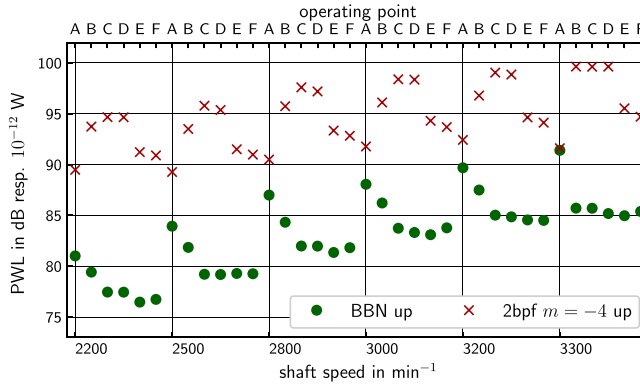


**Figure 7.** Modal sound power of the Tyler–Sofrin mode and broadband noise for all test points.

The modal sound power levels of all upstream propagating modes with radial mode order  $n = 0$  are shown. The highest sound power levels are emitted at BPF and two BPF, although the RSI mode is cut off at BPF. In the average rotor-locked spectrum in Figure 5, multiple pure tones around two BPF at engine orders 30–39 are visible. The results of the mode analysis show that the azimuthal mode order of these tones is  $m = V - \text{engine order}$ . One possible reason for these tones might be due to irregularities in the rotor wakes,<sup>9</sup> which can arise from the combination of inflow distortion and irregularities in the rotor blades. As the Reynolds number of the blades is relatively low (88k @70% of blade span),<sup>29</sup> it is expected that the boundary layer transition from laminar to turbulent might happen at different chord length positions from blade to blade, leading to non-identical rotor blade wakes. Meyer et al.<sup>30</sup> showed, by means of hot-wire measurements for a different fan, that indeed the velocity deficit differs from blade to blade not only statistically but also in the ensemble average as well. It is assumed that small deviations in the blade geometry cause the differences between individual wakes. For that configuration also a step-like azimuthal mode pattern was found in acoustic measurements that was connected to the wake irregularities. It was shown that the resulting rotating pressure distribution scattered in the respective engine orders through the Doppler shift.<sup>31</sup>

The inflow distortions that remain in the inflow in spite of the ICD, the geometric irregularities of the blades, and the rotor wake inhomogeneities are still to be investigated. This is however outside the scope of the present work. The authors argue, however, that the same mechanism is the source of the extra “spurious” tones in the rotor-locked spectrum in Figure 6(a).

In Figure 6(b), the modal sound power levels of all modes at engine order 36 are shown. The sign behind the radial mode order indicates the propagation direction of the mode, that is, ‘-’ for up- and ‘+’ for downstream propagation. Note the different scaling of the color bar. The RSI tone at  $m = -4$  is about 20 dB above all other modes.

In order to compare all the operating points, the modal sound power of the upstream propagating RSI tone at two BPF is shown in Figure 7 for all operating points.

At all rotor speeds, the same pattern is repeated for the RSI mode. The maximum power level is found for the flow coefficient  $\phi = 0.21$ , letter C. The tonal RSI noise is strongly affected by radial dephasing of the tilted rotor wakes which leads to destructive interferences.<sup>6</sup> This effect is driven by the three dimensional geometries of the rotor and stator blades and is presumed to cause the less effective excitation at the lower flow rates (A and B). The power level of the RSI tone additionally depends on the velocity deficit and the width of the rotor wakes, which scale with the relative flow speed. This explains the overall increase with higher rotor speed. At constant rotor speed, with

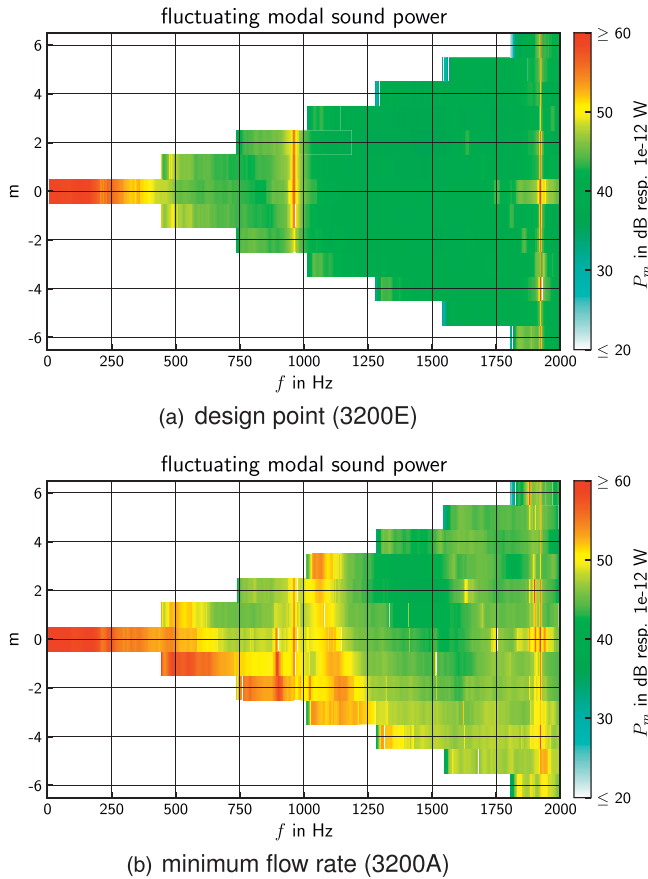


**Figure 8.** Modal sound power of upstream propagating modes, sum over all propagating radial modes.

increasing flow rate, the flow incidence angle decreases. With decreasing incidence also the rotor wake width and velocity deficit decrease<sup>32</sup>; therefore, the noise is reduced with higher flow rate. This effect can be shown for higher flow coefficients (C to F). The incidence varies from  $5^\circ$  at the smallest flow coefficient to  $-1^\circ$  at the highest flow coefficient.

To reduce the tonal noise emission, it seems desirable to operate the fan at the lowest possible loading. As this is not possible in every application, the shape of the blades can be designed to reach a reduction of tonal noise emissions.<sup>33</sup> The relation between the tonal noise emission and incidence is not monotonic, which implies that the operating condition with minimum tonal noise is potentially shifted by changing the blade design.

**Broadband Mode Analysis Results.** The cross-modal matrix is calculated by solving equation (3). In Figure 8, the results of the broadband RMA are visualized for two fan operating points. Depicted is the modal sound power level of upstream propagating modes summed over all propagating radial modes. At first glance, the modal broadband noise spectrum seems much smoother at the fan design point, where the modal distribution is rather symmetric (Figure 8(a)). On the contrary, the spectrum

**Table 2.** Scaling law exponent.

$\Phi$	0.19	0.20	0.21	0.22	0.24	0.26
$\eta(2 \text{ BPF})$	1.74	2.94	2.84	2.91	2.53	2.33
$\eta(\text{BBN})$	5.64	4.29	4.84	4.61	4.89	4.98

referring to the operating point with low mass flow (low flow coefficient) and high pressure ratio exhibits more spectral components and the modal distribution is more asymmetric (Figure 8(b)).

In order to calculate the overall broadband noise sound power level, the frequency spectra were integrated between the engine orders 7 and 37. The lower limit was used to exclude the low-frequency band, which presumably does not originate from the fan. The higher limit is necessary because of the frequency limit of the microphone array. The overall sound power levels of all operating points are shown in Figure 7.

With a least squares fit assuming  $P \propto M_{\text{tip}}^n$ , the scaling law exponent for the broadband noise and the RSI tone at different flow rates are calculated.<sup>8</sup> The results are summarized in Table 2. The broadband noise scales approximately with the empirical reference value 5, but the RSI tone scales with a much smaller factor. Note that for the lowest flow coefficient, the scaling exponent for the RSI tone reaches a minimum while the scaling exponent of the broadband noise reaches a maximum. These operating points are close to the surge line and have the least stable flow field. This could explain the high scaling of the broadband noise and the low scaling of the RSI tone. Regarding the sound power at a constant rotor speed, a repetitive pattern is visible. At small flow rates, the broadband sound power decreases with the flow rate (A to C) and remains rather constant at higher flow rates (C to F). In the following section, this trend in the broadband noise will be reproduced by means of simulated measurements, where only the source mechanisms of broadband RSI and inflow-rotor interaction are modeled.

### Analytical Modeling

The general procedure of the theoretical source models is based on a mean line approach: The steady and unsteady aerodynamic parameters are calculated at one radial position and then radially extrapolated. In a first step, the model of the fan was adjusted. In this step, the blade angles of rotor and stator leading and trailing edges are iteratively changed and converge to representative angles. With these angles, the same corrected mass flow and pressure ratio are calculated by the model at the design point, as were obtained from a numerical Reynolds-averaged Navier–Stokes (RANS) simulation. The focus lies on aerodynamic similarity between measurements and simulations, rather than geometric similarity.

The trade-off of this approach is that the representative angles are not the same as the actual blade angles. As discussed above, the geometry of the rotor blades and stator vanes has a critical influence on tonal noise excitation. Hence, larger deviations in the characteristics of the simulated and measured tonal noise are expected. The broadband noise sources are presumed to better reproduce the measured trends because they depend mainly on aerodynamic parameters extracted from measurements, such as Mach number, turbulence intensity and ILS, that vary with the operating point. The relevant geometric properties are the blade thickness, angles and chord length.

The different sound sources like rotor–stator interaction noise, inflow-rotor, inflow-stator interaction noise, as well as rotor and stator trailing edge noise are predicted with theoretical models. The simulation is based on Goldstein<sup>34</sup>'s solution of the acoustic analogy with moving solid

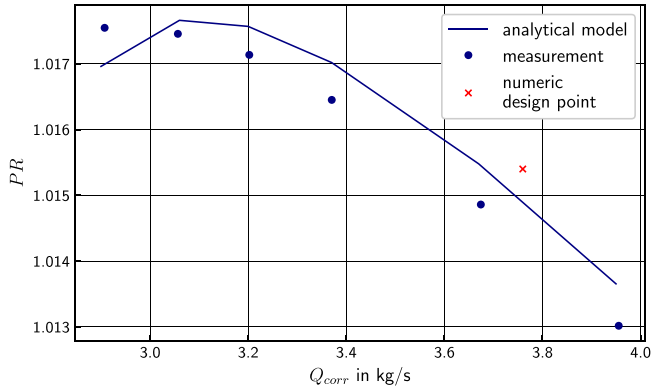


**Figure 9.** Pressure ratio comparison of measurements and model.

boundaries. The aerodynamic properties such as mean flow speed, wake properties, and turbulence are estimated on the basis of a semi-empirical mean line method.<sup>3</sup>

In Figure 9, the pressure ratio and mass flow for six operating conditions at 3200 r/min are shown. The operating conditions from the RANS calculation at the design point predict a higher pressure ratio than the measurement shows. Hence, the results from the analytical simulation also predict a higher pressure ratio. At low mass flows, the predicted pressure ratio is lower than the measured pressure ratio. This operating condition is close to the surge line and is difficult to model with the mean line approach. It shall be noted, that the theoretical source models were originally developed and tested for full-scale fans with high pressure ratios. Taking that into account, the predicted and measured operating conditions match reasonably well.

The essential input parameters of the source models are the mean flow velocity, the turbulent kinetic energy (TKE), and integral length scale (ILS). The former was measured with a dynamic pressure tube in the inlet, whereas the estimation of the TKE and ILS is described in the next section.

*Estimation of the Turbulence Input Parameters.* The turbulence parameters TKE and ILS were extracted from instationary aerodynamic measurements by means of hot-wire anemometry. Measurements were carried out in the same test rig, however with a different fan. A detailed report of this measurement was published by Oertwig<sup>14</sup> and selected results also by Caldas et al.<sup>26</sup> As the inlet Mach numbers measured in that work (approx. 16.5 m/s) are roughly the same as in the current work (18 m/s), average numbers for turbulence quantities shall be used from that measurement campaign.

In the work from Oertwig,<sup>14</sup> four hot-wire probes were installed on the fan rig duct wall, 90° apart and 440 mm (around one duct-diameter) upstream of the fan. Each probe comprises of two hot-wire elements. In this work, only the axial component is analyzed. Three measured radial positions were 45 mm, 112 mm, and 192 mm from the duct outer casing wall with 453 mm in diameter. Acquisition time was set as 10 s at 80 kHz sampling frequency. Unfortunately, no hot-wire measurement was performed inside the boundary layer. However, a refined measurement was carried out along the radial direction with a Prandtl-tube where the boundary layer thickness could be estimated as about 20 mm for a mean flow of 16.4 m/s. It is known that the turbulence in the boundary layer reaches values up to 5–6 % in intensity but decays rapidly in the external region of the boundary layer.<sup>35–37</sup>

In order to get a better estimation of the overall average turbulence levels as well as the average TKE to be used as input for the simulation, a typical boundary layer turbulence profile measured in

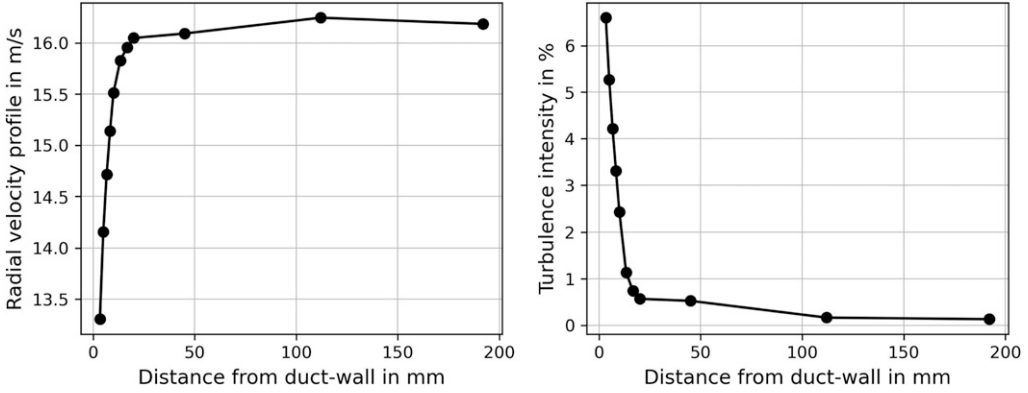


**Figure 10.** On the left-hand side is the radial velocity profile. Right-hand side shows the radial turbulence profile at the inlet. Fan speed at 3200  $r/min$ .

other test rigs<sup>36–39</sup> was used and scaled down to the current Mach number. Results for velocity profile and turbulence levels are seen in Figure 10.

The root-mean-square (RMS) of the fluctuating velocity component  $\tilde{u}$  was obtained by integrating the power spectrum density (PSD) of the axial velocity component, such as shown in Figure 11. The turbulence intensity is defined as the ratio between the fluctuating and the mean velocities:  $Tu = \frac{\tilde{u}}{U_x}$ . This plot shows the PSD for data measured at the same plane and four angular positions,  $90^\circ$  apart and at a radial distance of 112 mm from the wall. The TKE could be then estimated according to the definition<sup>35</sup>:  $TKE = \frac{3}{2}\tilde{u}^2$ . For the ILS however, instead of using the definition which relies on the integral of the autocorrelation function of the velocity component,<sup>35</sup> a von-Kármán spectrum was fitted to the estimated PSD from measured hot-wire data. The corresponding ILS of this fit was then used as the estimated ILS value for the corresponding measured record. This approach is used instead of the classical autocorrelation function integral because of the sensitivity of the latter to low-frequency disturbances as well as eventual tones in the spectrum, which are not meant to be turbulence related, as shown by Caldas et al.<sup>40</sup>

The average values for TKE and ILS were then obtained by first an average in the circumferential direction, followed by a weighted average by the radial position and by the axial velocity  $U_x$

$$TKE = \frac{\int_0^R TKE(r) U_x(r)^2 r dr}{\int_0^R U_x(r)^2 r dr} \quad (5)$$

$$ILS = \frac{\int_0^R ILS(r) U_x(r)^2 r dr}{\int_0^R U_x(r)^2 r dr} \quad (6)$$

Substituting the values obtained from the measurements, as well as the approximated boundary layer profile extracted from other similar test rigs and scaled down, we obtain the following

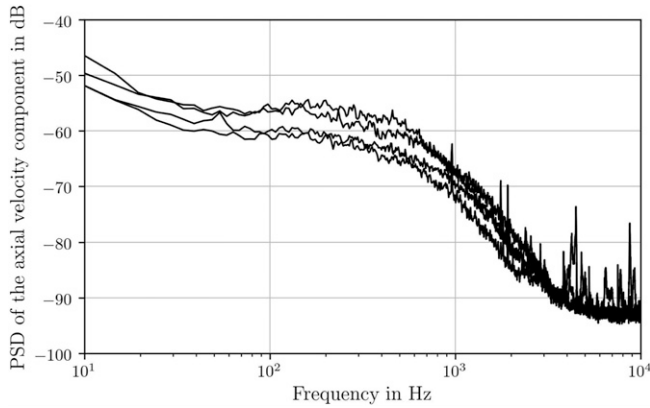


**Figure 11.** Power spectral density (PSD) of the axial velocity component at the inlet measured at four different circumferential positions at a fan speed of 3200 r/min.

numbers:  $TKE = 0.1 \text{ m}^2/\text{s}^2$ ,  $Tu = 1.2\%$ , and  $ILS = 13 \text{ mm}$ . In the present study, the values of TKE and ILS are assumed constant for different operating points.

## Results

In this study, only the tonal and broadband rotor–stator interaction (RSI) and the broadband noise emitted by the turbulent inflow–rotor interaction are shown, as these are the dominant calculated noise sources.

Figure 12 compares the measurement and analytical results for different flow rates at rotor speed 3200 r/min. In the tonal results, only the RSI mode at two BPF is considered, as no propagating mode is calculated in the idealized model at BPF in accordance with Tyler and Sofrin.<sup>12</sup> The tone at two BPF first increases, then decreases with higher flow rate. The maximum of emitted sound power is at different flow rates for measurement and analytic results. The tonal RSI noise arises from the periodic collisions of the turbulent rotor wakes with the stator leading edges which can be represented by a dipole distribution. As the energy of the rotor wakes decreases with higher flow coefficients owing to the reduced rotor blade incidence and aerodynamic loading, the source strength of the RSI noise also decreases with higher flow coefficients. This effect can explain the decrease in the tonal sound power at the higher flow coefficients. The swirl behind the rotor changes with the flow rate as the rotation speed remains constant while the mass flow changes. This affects the way that the wakes are twisted in the interstage area. The wakes hit the stator leading edge at different times for different radii, which leads to destructive interferences. Which might be even more relevant as only one radial mode order is propagating at two BPF. The larger deviations in the two BPF tone at smaller flow coefficients are suspected to be caused by differences in the angles and radial shapes of the rotor blades and stator vanes between simulation and experiment. In the scope of this study however, this relation is not further analyzed. Here, two broadband sources are assumed to be dominant and therefore considered: The broadband RSI noise and the interaction of turbulence in the inlet with the rotor. With increasing flow rate, meaning a decrease in incidence, the broadband RSI noise decreases, as the width of the wakes and the turbulence intensity therein are reduced.<sup>32</sup> The reason for this effect is the reduced boundary layer thickness on the blades. This is due to a shift of the laminar to turbulent transition point on both blade sides toward the trailing edge.<sup>41</sup> In contrast

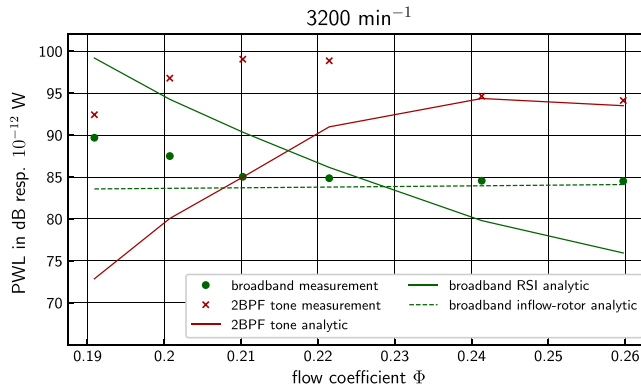


**Figure 12.** Measured and calculated sound power level at different flow rates.

to the tonal RSI, no destructive interferences can occur, since the simulated sources are uncorrelated. Hence, broadband RSI noise is expected to decrease continuously as the flow coefficient grows.

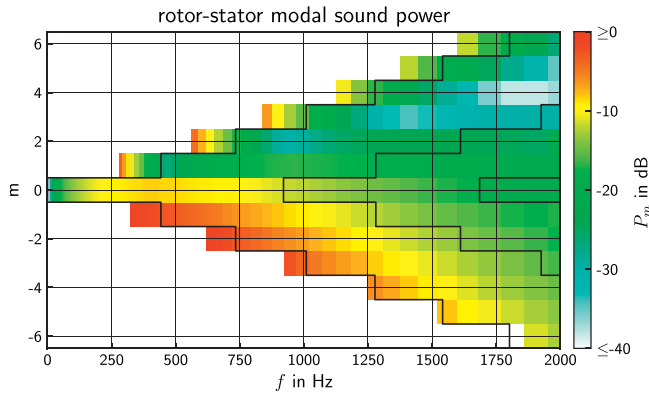
The inflow-rotor interaction noise scales with the TKE. In the current study, the TKE is assumed constant at all operating points. The measured broadband noise decreases, then a plateau is reached. As presumed, this trend can be reproduced by summation of the two simulated sources. The calculated broadband rotor–stator interaction noise continuously decreases with higher flow rates, as the rotor wakes become narrower. The calculated inflow-rotor noise remains almost constant at all flow rates and becomes a relevant source at higher flow rates, as the RSI noise further decreases.

In Figure 13(a), the upstream propagating modal distribution of the calculated RSI broadband noise and in Figure 13(b) the calculated inflow-rotor noise are depicted. It should be noted that the mode distribution is calculated at the source location. The spinner, the hub, and the flow swirl in the interstage section have an impact on the modes, especially on the cut-on frequencies. The cut-on frequencies in the measurement section with no hub and no swirl are marked with solid lines. The broadband RSI noise is excited with high amplitudes at frequencies, where the propagating mode is cut-on in the interstage area, but cut off in the measurement section. This propagation effect is not considered in the results shown in Figure 12 and could be the origin of the overestimation at small flow coefficients of the broadband RSI noise compared to the measured broadband noise. The inflow-rotor noise also excites modes with high amplitudes that are not able to propagate into the measurement section.

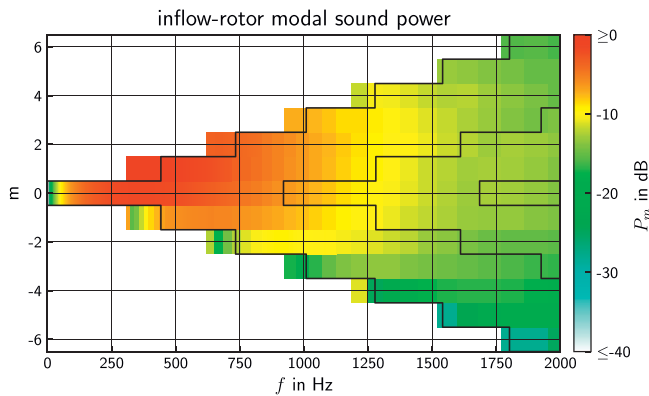
It should be noted that scattering and shielding effects at the rotor are not taken into account in the model. However, mode scattering effects at the rotor can be neglected, as the super-resonance criterion of Kaji and Okazaki<sup>42</sup> is not reached until about 2200 Hz. Shielding effects of the rotor also have an effect on the propagation, but are not considered in the analytical calculations. Modes with positive spinning direction are shielded by the rotor, as they rotate in opposite directions.<sup>43</sup> This is in agreement with the measurements at low flow coefficients that show higher amplitudes for modes with negative spinning direction. At higher flow rates however, the mode distribution is rather symmetric.

As shown in Figure 13, the two sources have a very pronounced modal distribution which is mainly driven by the dipole axis on the leading edge of the blades and vanes, respectively.

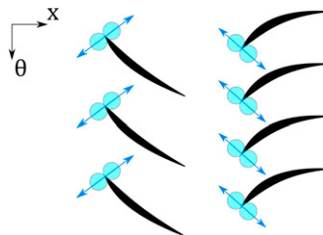
This relation is illustrated with the help of Figure 14. Let us consider a dipole at the leading edge of the rotor: Its main radiation directions are in positive  $\theta$ -direction for upstream propagation, and in negative  $\theta$ -direction for downstream propagation. Therefore, at the rotor-leading edge, upstream



(a) Broadband RSI noise.



(b) Inflow-rotor interaction noise.

**Figure 13.** Modal distribution of the calculated broadband noise sources at test point 3200A ( $\Phi = 0.19$ ).**Figure 14.** Sketch of the dipole axes at the rotor- and stator-leading edges.

propagating modes with positive spinning direction ( $m > 0$ ) are exited at higher amplitudes than modes with negative spinning direction ( $m < 0$ ), and vice versa at the stator-leading edge. Note that the profiles shown in Figure 14 are only for the sake of visualization and do not resemble the real profiles of the fan. A visual comparison shows that the measured mode distribution at low flow



coefficients in Figure 8(b) looks rather similar to a mode distribution of the RSI simulation as depicted in Figure 13(a), while at higher flow coefficients the measured mode distribution in Figure 8(a) shows similarities with the inflow-rotor interaction simulation results in Figure 13(b). Some remaining spectral components cannot be uniquely matched to a specific source mechanism. The simulation results show the plausibility that the broadband RSI and inflow-rotor interaction are the dominant noise sources. It seems that the rotor–stator interaction is the dominant broadband noise source at low flow coefficients, while at high flow rates the inflow-rotor noise contributes relevant sound power levels.

Further broadband sources could also contribute to the overall sound power. For example, numeric simulations showed a flow separation at the stator trailing edge close to the hub. In a first estimation with the analytical model, the trailing edge noise of rotor and stator is calculated to be about 10 dB below the other sources.

## Conclusion

A new Blisk rotor was implemented in the test rig and the aerodynamic performance is measured to be in accordance to the prediction with an analytical approach.

The analysis of fan noise measurements remains a challenging task. The rotor-locked tones that arise from rotor–stator interaction are sensitive to changes of the blade loading and larger deviations of the amplitude occur to theoretical prediction. The broadband spectrum is difficult to analyze because multiple sources radiate noise with fluctuating phase in the same frequency bands with similar amplitudes. Yet, some conclusions can be drawn from the presented results”

1. The dominant tone is the two BPF Tyler–Sofrin mode as would be expected. The one BPF tone is also excited, although it is cut off. This implies inflow disturbances in spite of an inflow control device. Further improvement of the flow condition is proposed for further investigations. In this regard, a new ICD was designed to reduce non-representative noise excitation in future experiments.<sup>26,44</sup>
2. A step-like pattern is found in the mode analysis of the tones around two BPF that results from deviations between individual rotor blade wakes. Further research is suggested to clarify whether these wake deviations are a result of inflow disturbances or due to manufacturing tolerances.
3. The tonal noise amplitude of two BPF is the lowest at off-design conditions, either very high or very low loading. This implies a potential design conflict between fan performance and acoustic optimization.
4. Depending on the flow coefficient, the tonal noise in the inlet scales with the Mach number to the power of 1.7–2.9, while the broadband noise scales with the Mach number to the power of 4.3–5.6. Therefore, the broadband noise must be considered at higher Mach numbers.
5. The measured broadband noise mode spectrum is symmetric and planar at the design point. At off-design however, the mode distribution is asymmetric and the spectrum contains frequency bands with elevated sound power. It is assumed that different source mechanisms dominate at these operating points.
6. The geometry of the rotor wakes is modeled based on center line. The tonal RSI noise is sensitive to changes in the geometry of the wakes. Therefore, larger deviations are found between the acoustic and experimental results. To accurately model the tonal noise sources, CFD simulations or measurements of the rotor wakes are deemed necessary.

7. For the analysis of broadband noise, the theoretical model was used on the basis of the non-stationary flow field, which was reasonably estimated from former measurements. Based on the modal distribution of the calculated sources, the two dominant broadband noise sources are plausibly identified to be broadband RSI noise at low flow rates and inflow-rotor noise at high flow rates. The expected fan-operating conditions should thus be considered in the design of low-noise fans.

Although numerous simplifications made with the mean line approach, the simulations predicted the general trends fairly well. The stationary flow field is measured at only one position and the turbulence is only estimated on the basis of comparable measurements. The findings of this study will help to set up test plans of future experiments, that are planned at a new test rig with optimized aerodynamic conditions at higher rotor speeds and mass flows. The new test rig includes an improved inflow control device to reduce the inhomogeneity of the flow field and extensive microphone arrays, allowing acoustic analysis at higher frequencies.<sup>44</sup> An additional array downstream of the stator will be implemented, possibly turning the spotlight on other source mechanisms such as rotor or stator trailing edge noise. Thus in upcoming studies the research questions that arise from this study will be pursued.

### Declaration of conflicting interests

The author(s) declared no potential conflicts of interest with respect to the research, authorship, and/or publication of this article.

### Funding

The author(s) received no financial support for the research, authorship, and/or publication of this article.

### ORCID iD

Lukas Klähn  <https://orcid.org/0000-0002-1425-4453>

### References

1. Tapken U, Pardowitz B and Behn M. Radial mode analysis of fan broadband noise. In: 21st AIAA/CEAS Aeroacoustics Conference. Dallas, TX (USA), 2017. AIAA 2017–3715.
2. Bräunling WJG. *Flugzeugtriebwerke*. 3 ed. Springer-Verlag Berlin Heidelberg, 2009.
3. Moreau A. *A unified analytical approach for the acoustic conceptual design of fans of modern aero-engines*. PhD Thesis. Technical University Berlin, 2017. DLR research report DLR-FB-2017-56.
4. Jaron R. *Aeroakustische Auslegung von Triebwerksfans mittels multidisziplinärer Optimierungen*. PhD Thesis. Technical University of Berlin, 2018.
5. Jaron R, Moreau A, Guérin S, et al. Optimization of Trailing-Edge Serrations to Reduce Open-Rotor Tonal Interaction Noise. *J Fluids Eng* 2018; 140(2). DOI: [10.1115/1.4037981](https://doi.org/10.1115/1.4037981).
6. Moreau A, Aulich AL, Jaron R, et al. Optimization of casing contours in an aero-engine fan stage with emphasis on rotor-stator interaction noise. *16th International symposium on transport phenomena and dynamics of rotating machinery*. Honolulu, United States, 2016.
7. Enghardt L, Kausche P, Moreau A, et al. Active control of fan tones by means of trailing edge blowing. In: 21st AIAA/CEAS Aeroacoustics Conference. Dallas, TX, 2015. AIAA 2015–2828. DOI: [10.2514/6.2015-2828](https://doi.org/10.2514/6.2015-2828).

8. Stephens DB and Morris SC. The effect of blade loading on sound sources in a ducted rotor. In: 12th AIAA/CEAS Aeroacoustics Conference. Cambridge, MA, 2006. AIAA 2006–2683.
9. Moreau A, Enghardt L and Bodén H. *Fan noise 2007 - 3rd international symposium on fan noise*. Lyon, France, 2007. On the relation between broadband noise and fan aerodynamic performance
10. Guérin S, Moreau A and Tapken U. Relation between source models and acoustic duct modes. In: 15th AIAA/CEAS Aeroacoustics Conference. Miami, FL, 2009. AIAA 2009–3364.
11. Carolus T. *Ventilatoren: aerodynamischer entwurf – konstruktive lärminderung – optimierung*. 4 ed. Wiesbaden, Germany: Springer Vieweg, 2020.
12. Tyler JM and Sofrin TG. Axial flow compressor noise studies. In: *SAE Technical Paper*, 1962. DOI: [10.4271/620532](https://doi.org/10.4271/620532).
13. Banzhaf HU, Carolus T, Schneider M, et al. Kombiniertes aerodynamisches und akustisches Kennfeld zur Auswahl wirkungsgrad- und geräuschoptimaler Axialventilatoren. In: *VDI-fachtagung Ventilatoren*. Brunswick, Germany, 2006.
14. Oertwig S. *Optimierung der Einlaufströmung an einem Axialventilator-Versuchsstand und deren Einfluss auf die Akustik*. Master thesis. Berlin: Technische Universität Berlin, 2016.
15. Jaron R. *Vorauslegung einer Rotor-Stator Stufe mit Hilfe von semi-analytischen Tools* Studienarbeit. Technische Universität Berlin, 2010.
16. Lieblein S. *Vi - experimental flow in two-dimensional cascades*. Technical Report NACA-RM-E55K01a, 1965. Aerodynamic design of axial-flow compressors
17. de Haller P. Das Verhalten von Tragflügeln in Axialverdichtern und im Windkanal. Probleme der Strömungstechnik im Maschinenbau. *Tech Rep VDI-Berichte* 1955; 3.
18. Lieblein S, Schwenk F and Broderick R. *Diffusion factor for estimating losses and limiting blade loadings in axial-flow-compressor blade elements*, 1953.
19. Wismer NJ. *Time domain averaging combined with order tracking*. Application Note. Denmark: Brüel & Kjaer (nd), 2003. Obtained from website, <http://www.bksv.com>.
20. Antoni J. Cyclostationarity by examples. *Mech Syst Signal Process* 2009; 23(4): 987–1036.
21. Grizewski L, Behn M, Funke S, et al. Cyclostationary analysis of fan noise influenced by an inflow control device. *AIAA J* 2021; 59(7): 2578–2589. DOI: [10.2514/1.J059493](https://doi.org/10.2514/1.J059493).
22. Tapken U and Enghardt L. Optimisation of sensor arrays for radial mode analysis in flow ducts. In: 12th AIAA/CEAS Aeroacoustics Conference (27th AIAA Aeroacoustics Conference). Cambridge, MA (USA), 2006. AIAA 2006–2638.
23. Hanson DB. Broadband noise of fans - with unsteady coupling theory to account for rotor and stator reflection/transmission effects. In: *Contractor Report NASA/CR-2001-211136, NASA*. Glenn Research Center, 2001.
24. Morfey CL. Sound transmission and generation in ducts with flow. *J Sound Vibration* 1971; 14(1): 37–55. DOI: [10.1016/0022-460X\(71\)90506-2](https://doi.org/10.1016/0022-460X(71)90506-2).
25. Tapken U, Gutsche D and Enghardt L. Radial mode analysis of broadband noise in flow ducts using a combined axial and azimuthal sensor array. In: AIAA Aviation - 20th AIAA/CEAS Aeroacoustics Conference. Atlanta, USA, 2014. AIAA 2014-3318.16-20.06.2014
26. Caldas LC, Oertwig S, Rudolphi A, et al. Development and assessment of an inflow control device and a bell-mouth for a low-speed aeroacoustic fan rig. In: 25th AIAA/CEAS Aeroacoustics Conference 2019. Delft, The Netherlands, 2019. AIAA 2019–2713.
27. Rice EJ, Heidmann MF and Sofrin TG. *Modal propagation angles in a cylindrical duct with flow and their relation to sound radiation*. NASA Technical Memorandum, 1979, p. 79030.
28. Schade S, Jaron R, Moreau A, et al. Tonal noise reduction mechanisms of low-count ogv designs. In: Delft International Conference on Urban Air-Mobility. Delft, The Netherlands: DICUAM, 2021.
29. Lauchle GC. *Centrifugal and axial fan noise prediction and control*, 2007.

30. Meyer R, Hakansson S, Hage W, et al. Instantaneous flow field measurements in the interstage section between a fan and the outlet guiding vanes at different axial positions. In: 13th European Conference on Turbomachinery Fluid Dynamics & Thermodynamics 2019. Madrid, Spain, 2019, DOI: [10.29008/ETC2019-330](https://doi.org/10.29008/ETC2019-330).
31. Behn M and Tapken U. Investigation of sound generation and transmission effects through the acat1 fan stage using compressed sensing-based mode analysis. In: 25th AIAA/CEAS Aeroacoustics Conference 2019. DOI: [10.2514/6.2019-2502](https://doi.org/10.2514/6.2019-2502).
32. Lakshminarayana B, Govindan TR and Reynolds B. Effects of rotation and blade incidence on properties of turbomachinery rotor wake. *AIAA J* 1982; 20(2): 245–253. DOI: [10.2514/3.51072](https://doi.org/10.2514/3.51072).
33. Carolus T and Beiler M. Skewed blades in low pressure fans - a survey of noise reduction mechanisms. In: 3rd AIAA/CEAS Aeroacoustics Conference 1997: 47–56. DOI: [10.2514/6.1997-1591](https://doi.org/10.2514/6.1997-1591).
34. Goldstein M. Unified approach to aerodynamic sound generation in the presence of solid boundaries. *The J Acoust Soc America* 1974; 56(2): 497–509. DOI: [10.1121/1.1903283](https://doi.org/10.1121/1.1903283).
35. Hinze JO. *Turbulence*. McGraw-Hill, 1975.
36. Meyer R, Knobloch K and Hakansson S. Hot-wire measurement in a direct driven high speed turbo fan (ddtf) rig. In: 11th European Turbomachinery Conference. Madrid, Spain, 2015. ETC–11–256.
37. Meyer R, Knobloch K and Linden J. Hot-wire measurement in a high speed counter rotating turbo fan rig. In: *ASME Turbo Expo*. Glasgow, UK, 2010, pp. 247–254.
38. Lengyel-Kampmann T, Bischoff A, Meyer R, et al. Design of an economical counter rotating fan: comparison of the calculated and measured steady and unsteady results. In: *ASME Turbo Expo*. Copenhagen, Denmark, 2012, pp. 323–336.
39. Meillard L, Schnell R, Meyer R, et al. *Time resolved pressure and velocity measurements at the dlr uhbr-fan and comparison with simulation data*. Stuttgart, Germany: Deutscher Luft- und Raumfahrt-kongress, 2013, p. 62. In
40. Caldas L, Kissner CA, Behn M, et al. Comparison of techniques for the estimation of flow parameters of fan inflow turbulence from noisy hot-wire data. In: *AIAA AVIATION 2021 FORUM*, 2021. DOI: [10.2514/6.2021-2487](https://doi.org/10.2514/6.2021-2487).
41. Solomon WJ and Walker GJ. Incidence effects on wake-induced transition on an axial compressor blade. *J Propulsion Power* 2000; 16(3): 397–405. DOI: [10.2514/2.5603](https://doi.org/10.2514/2.5603).
42. Kaji S and Okazaki T. Propagation of sound waves through a blade row. *J Sound Vibration* 1970; 11(3): 355–375.
43. Hanson DB. *Acoustic reflection and transmission of 2-dimensional rotors and stators including mode and frequency scattering effects*. research report NASA/CR-1999-208880, NASA. Glenn Research Center, 1999.
44. Tapken U, Caldas L, Meyer R, et al. Fan test rig for detailed investigation of noise generation mechanisms due to inflow disturbances. In: *AIAA AVIATION 2021 FORUM*, 2021. DOI: [10.2514/6.2021-2314](https://doi.org/10.2514/6.2021-2314).

## Appendix

### Nomenclature

$a$	mode amplitude vector in Pa
$B$	blade number
Blisk	blade integrated disk
BPF	blade passing frequency
$c$	speed of sound in m/s
ICD	inflow control device

---

ILS	integral length scale
$m$	azimuthal mode order
$M$	Mach number
$n$	radial mode order
$\mathbf{p}$	pressure vector in Pa
$PR$	total pressure ratio
PSD	power spectrum density
$PWL$	sound power level in dB re $10^{-12}$ W
$Q_{\text{corr}}$	corrected mass flow in kg/s
$R$	duct radius in m
RMS	root mean square
RSI	rotor–stator interaction
$\mathbf{S}_{aa}$	cross-modal matrix in Pa <sup>2</sup>
$\mathbf{S}_{pp}$	cross-power spectral matrix in Pa <sup>2</sup>
TKE	turbulent kinetic energy
$U_x$	axial mean flow velocity in m/s
$V$	vane number
$\mathbf{W}$	mode transfer matrix
$A_{mn}^{\pm}$	mode amplitude in Pa
$P_{mn}^{\pm}$	modal sound power in W
$\tilde{u}$	fluctuating velocity component in m/s
$\eta$	scaling law exponent
$\phi$	flow coefficient
$\rho$	density in kg/m <sup>3</sup>
$\alpha_{mn}$	mode cut-on factor